

Iodocuprate Hybrids

Quaternary Phosphorus-Induced Iodocuprate(I)-Based Hybrids: Water Stabilities, Tunable Luminescence and Photocurrent Responses

Wen-Ting Zhang,^[a] Jian-Zhi Liu,^[b] Jing-Bo Liu,^[b] Kai-Yue Song,^[a] Yi Li,^[a] Zhi-Rong Chen,^[a] Hao-Hong Li,^{*[a]} and Rong Jiang^{*[a]}

Abstract: Four (triphenyl)phosphonium-based quaternary phosphorus salts with different substituents (varying from methyl to *n*-butyl) were selected to be structural directing agents (SDAs) to construct four iodocuprate(I) hybrids via solution method, i.e., [(PPh₃Me)(Cu₃I₄)]_n (**1**), [(PPh₃Et)(Cu₃I₄)]_n (**2**), [(PPh₃*i*Pr)₂(Cu₂I₄)] (**3**), [(PPh₃*n*Bu)(Cu₃I₄)]_n (**4**). The inorganic iodocuprates in **1**, **2** and **4** are 1-D (Cu₃I₄)_nⁿ⁻ chains constructed from Cu₅I₁₁ units, but (Cu₂I₄)²⁻ in **3** is a di-nuclear cluster. Interestingly, the strength of Cu...Cu and π-π stacking interactions are weakened with the lengthening of alkyl groups on P-atom. The best water stability of **4** can be ascribed to the better hydrophobicity of *n*-butyl group, which deters the dispersing of

organic and inorganic moieties and as a result, inhibit hydrolysis reaction. Furthermore, all compounds exhibit typical reversible luminescent thermochromic behaviors, among which **4** exhibits blue emission and the quenching of higher energy (HE) zone in **1** and **2** are led by strong π-π stacking interactions. Besides, effective and repeatable photocurrent responses can be detected in these compounds. In all, by systematically introducing alkyl groups into (triphenyl)phosphonium as SDAs to prepare hybrid iodocuprates, we can find that the longer alkyl groups can achieve stronger tunable PL materials with enhanced water stabilities.

Introduction

Luminescent materials are one of the most important materials due to their wide applications in display visualization devices, trace detection, chemical sensing, biological labeling, et al.^[1,2] In this realm, cuprous iodide-based photoluminescence (PL) materials have captured special interests owing to their extraordinary structural diversity and large variety of photophysical properties,^[3,4] and more importantly, their low cost and non-toxicity compared to the noble and rare-earth metals.^[5-7] So far, from the viewpoint of their structures, the cuprous iodide-based PL materials can be divided into two types: one is neutral iodocuprate components coordinated by neutral organic ligands (e.g., cubane-like [Cu₄I₄R₄]),^[8-11] the other is negative inorganic iodocuprate species accompanied by positively charged structure directing agents (SDAs), in which the iodocuprates range from low dimensional clusters, chains to extended 2-D and 3-D frameworks.^[12-14] In the former case, most of the neutral organic ligands are phosphine with different substituents on phosphorus or phenyl rings, such as [PPh₂(CH₂CH=CH₂)].^[9,15] And the luminescence behaviors of

this kind of (cluster-based) compounds are greatly determined by the compositions, geometries, nuclear numbers and metal...metal interactions.^[16-19] However, compared with the extensively reported cluster-based iodocuprates, the polymeric anionic iodocuprates are still underdeveloped due to lack of efficient synthetic strategies, and the commonly used structure directing agents (SDAs) are N/S-bearing organic cations with different skeleton flexibility, hydrophobicity and electronic structures,^[12,13,20,21] for example, methylnicotinohydrazide dication (MNH²⁺).^[12] The quaternary phosphorus salts were seldom utilized as SDAs in iodocuprate system, and only limited iodocuprates/quaternary phosphorus hybrids were reported.^[22-31]

For cluster-based iodocuprate PL materials, previous studies have shown that their LUMO energies are commonly localized on the phosphine ligands, while the HOMOs are occupied by metal centers.^[32-34] Therefore, the cationization of phosphine ligands can change their electronic structure to increase LUMO energies, and the polymerization of iodocuprate can augment the HOMO energies, consequently the emission maximum (λ_{\max}) might shift to deep-blue region with the enhanced HOMO-LUMO gaps. The strategy might help to improve the luminescence properties of iodocuprate-based PL materials. Besides, the alkyl modification on phosphine ligands can improve their water stability, which will obviously decrease the fabricating costs and elongate the working life of related devices.^[13,35] In this work, four kinds of (triphenyl)phosphonium-based quaternary phosphorus salts containing different substituents (varying from methyl to *n*-butyl) on P atoms were used as struc-

[a] College of Chemistry, Fuzhou University, Fuzhou, Fujian, 350116, China
E-mail: lihh@fzu.edu.cn
<https://chem.fzu.edu.cn>

[b] Department of Otorhinolaryngology, Fujian Medical University Union Hospital, Fuzhou, Fujian, 350001, China

Supporting information and ORCID(s) from the author(s) for this article are available on the WWW under <https://doi.org/10.1002/ejic.201800813>.

tural directed agents (SDAs) to synthesize four new iodocuprates(I) hybrids, i.e., $[(\text{PPh}_3\text{Me})(\text{Cu}_3\text{I}_4)]_n$ (**1**), $[(\text{PPh}_3\text{Et})(\text{Cu}_3\text{I}_4)]_n$ (**2**), $(\text{PPh}_3i\text{Pr})_2(\text{Cu}_2\text{I}_4)$ (**3**), $[(\text{PPh}_3n\text{Bu})(\text{Cu}_3\text{I}_4)]_n$ (**4**). They exhibit blue-to-red emission with good water stability, in addition, excellent photocurrent responses can be detected, and the mechanisms were discussed and verified by theoretical calculations.

Results and Discussion

Crystal Structures

Under the template of four structural directed agents (SDAs) with different substituents on P atoms, the iodocuprates(I) moieties exhibit structural dimensions from 0-D $(\text{Cu}_2\text{I}_4)^{2-}$ cluster (for **3**) to 1-D $(\text{Cu}_3\text{I}_4)_n^{n-}$ chains (for **1**, **2**, **4**). And the $(\text{Cu}_3\text{I}_4)_n^{n-}$ chains in **1**, **2** and **4** are isostructures. No hydrogen bonds can be found in all compounds, but C–H $\cdots\pi$ interactions can be observed for all compounds, π – π stacking interactions were only detected in **1** and **2**.

Structures of $[(\text{PPh}_3\text{Me})(\text{Cu}_3\text{I}_4)]_n$ (1**), $[(\text{PPh}_3\text{Et})(\text{Cu}_3\text{I}_4)]_n$ (**2**) and $[(\text{PPh}_3n\text{Bu})(\text{Cu}_3\text{I}_4)]_n$ (**4**):** Single-crystal X-ray diffraction analysis reveals that hybrid **1** and **2** crystallizes in the monoclinic system with space group $P2_1/c$, but space group of **4** is $Pbca$. The structure of **1** has been documented.^[27] All of them consist of 1-D $(\text{Cu}_3\text{I}_4)_n^{n-}$ chains and template cations PPh_3Me^+ / PPh_3Et^+ / PPh_3nBu^+ . The $(\text{Cu}_3\text{I}_4)_n^{n-}$ chains in **1**, **2** and **4** are isostructures, here we focus our attention on **1** to depict the crystal structure. Their asymmetric units contain three crystallographically distinct Cu^+ ions, four I^- ions and one cation. The Cu centers are all coordinated by four I^- ions to give distorted tetrahedral geometries. In **1**, Cu(1) is coordinated by two μ_3 -I [$\text{I}(2)$, $\text{I}(4)$] and two μ_4 -I [$\text{I}(1)$, $\text{I}(1)\#1$, $\#1 x, -y + 1/2, z-1/2$], and Cu(2), Cu(3) atoms are surrounded by one μ_2 -I [$\text{I}(2)$], two μ_3 -I [$\text{I}(2)$, $\text{I}(4)$] and one μ_4 -I [$\text{I}(1)$] (Figure 1a). The bond lengths of Cu– μ_2 -I and Cu– μ_3 -I range among 2.6382(11)–2.6691(11) Å and 2.6232(11)–2.7335(12) Å, respectively, and the Cu– μ_4 -I distances are in the range of 2.6901(11)–2.7201(11) Å (Table S1 in the ESI). The Cu–I distances follows the following approximate order: $d(\text{Cu}-\mu_4\text{-I}) > d(\text{Cu}-\mu_3\text{-I}) > d(\text{Cu}-\mu_2\text{-I})$. This trend can also be observed in other iodocuprate hybrids.^[36,37] Cu(1) I_4 , Cu(2) I_4 , Cu(3) I_4 , Cu(2) $\#14$ and Cu(3) $\#214$ ($\#1 x, -y + 1/2, z-1/2$; $\#2 x, -y + 1/2, z + 1/2$) tetrahedra are self-condensed by edge-sharing to generate a Cu_5I_{11} unit (Figure 1a). Neighboring Cu_5I_{11} units are connected into a 1-D $(\text{Cu}_3\text{I}_4)_n^{n-}$ chain via edge-sharing model along the c -axis (Figure 1b). Cu \cdots Cu distances of 2.8517(15)–2.9899(15) Å are comparable with the sum of van der Waals radii of 2.80 Å, indicating the presence of weak metal–metal interactions (Figure 1a). Some other similar 1-D $(\text{Cu}_3\text{I}_4)_n^{n-}$ chains have been reported, such as $[\text{Ph}_4\text{P}][\text{Cu}_3\text{I}_4]$, but its chain is based on face-sharing CuI_4 tetrahedra.^[25] The adjacent 1-D $(\text{Cu}_3\text{I}_4)_n^{n-}$ chains feature parallel packing along the c -axes, and PPh_3Me^+ cations locate among the space of 1-D anionic chains (Figure 1c). No hydrogen bonds can be observed between organic and inorganic moieties, and only electrostatic force contributes to the structural stabilization. In addition, π – π stacking interactions with centroidal distance of 3.588(5) Å between adjacent phenyl rings can be observed (Table S3).

C–H $\cdots\pi$ interactions can also be detected among adjacent phenyl groups (Table S4). Based on these weak interactions, a 1-D cationic chain is presented (Figure 1d). The 1-D $(\text{Cu}_3\text{I}_4)_n^{n-}$ chains, packing diagrams and 1-D cationic chains based on C–H $\cdots\pi$ interactions of **2** and **4** can be seen in Figure S3 and Figure S4.

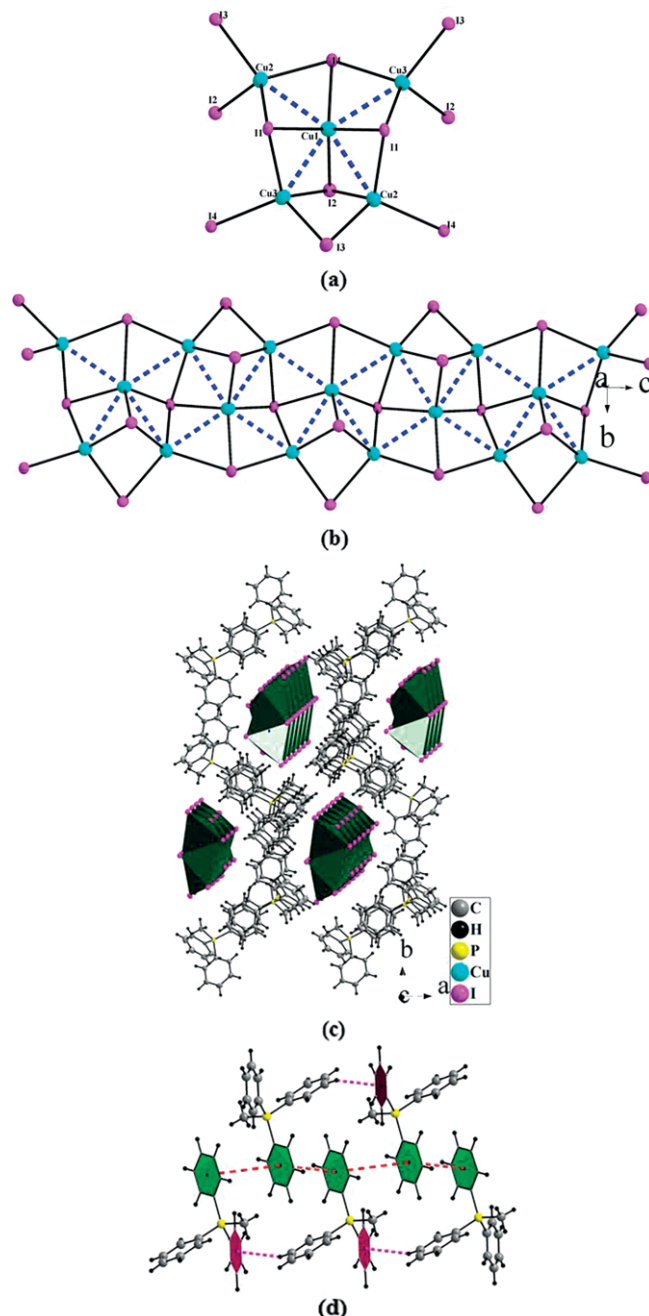


Figure 1. (a) Structure of Cu_5I_{11} unit showing Cu–Cu interactions; (b) 1-D $(\text{Cu}_3\text{I}_4)_n^{n-}$ chain based on edge-sharing CuI_4 tetrahedra; (c) packing diagram showing the position of SDAs; (d) 1-D cationic chain based on π – π stacking and C–H $\cdots\pi$ interactions in **1**.

From methyl substitution (PPh_3Me^+ in **1**) to n -butyl substitution (PPh_3nBu^+ in **4**), only structural perturbation happens on $(\text{Cu}_3\text{I}_4)_n^{n-}$ chains. The Cu \cdots Cu distances elongate to some extent [2.8356(17)–3.0591(16) Å for **2**, 2.8740(15)–3.0774(7) Å for **4**,

and π - π stacking interactions were also weakened with longer centroidal distance of 3.667(5) Å in **2**. When the substituent is *n*-butyl in **4**, no π - π stacking interactions can be found. The weakening of Cu...Cu and π - π stacking interactions in **1**, **2** and **4** might be led by larger counter cations. This trend again supports the conclusion that small counterions such as tetramethylammonium tend to produce infinite $[\text{Cu}_x\text{I}_y]^{(y-x)-}$ chains, but for larger counterions isolated clusters will generate.^[21]

The structural features of **1**, **2** and **4** are the presence of 1-D $(\text{Cu}_3\text{I}_4)_n^{n-}$ inorganic anionic chains with different Cu...Cu and π - π stacking interactions. Generally, in the iodocuprate system, tetrahedral (CuI_4) and triangular (CuI_3) may generate iodocuprate anions with the same simplest formula but exhibiting different real structures. For example, iodocuprate anions with the simplest formula of $(\text{Cu}_2\text{I}_3)^-$, including $(\text{Cu}_2\text{I}_3)^-$, $(\text{Cu}_4\text{I}_6)^{2-}$, $(\text{Cu}_{10}\text{I}_{15})^{5-}$ can exhibit 0-D, 1-D or 2-D structures. For 1-D $(\text{Cu}_3\text{I}_4)^-$ structures, several isomers including $[(\text{N}(\text{C}_3\text{H}_7))_4(\text{Cu}_3\text{I}_4)]_n$,^[21] $[(\text{etpy})(\text{Cu}_3\text{I}_4)]_n$,^[37] $[(\text{N-Bz-Py})_2(\text{Cu}_6\text{I}_8)]_n$,^[38] $[(\text{EtS}_4\text{C}_5\text{H}_4\text{NEt})(\text{Cu}_3\text{I}_4)]_n$,^[39] $[(\text{C}_{15}\text{H}_{14}\text{N})_2(\text{CuI}_2)(\text{Cu}_3\text{I}_4)]_n$,^[40] $[(\text{C}_3\text{H}_8\text{NO})(\text{C}_3\text{H}_7\text{NO})(\text{Cu}_3\text{I}_4)]_n$,^[41] $[(\text{C}_{24}\text{H}_{20}\text{P})(\text{Cu}_3\text{I}_4)]_n$,^[42] and $[(\text{C}_{24}\text{H}_{32}\text{KO}_8)(\text{Cu}_3\text{I}_4)]_n$ ^[43] have been reported, which were constructed by different connections of tetrahedral (CuI_4) and triangular (CuI_3) units. For instance, Cu_3I_4^- in $[(\text{N-Bz-Py})_2(\text{Cu}_6\text{I}_8)]_n$ are 3-D network, comparably, $[(\text{EtS}_4\text{C}_5\text{H}_4\text{NEt})(\text{Cu}_3\text{I}_4)]_n$ shows an infinite 1D chain constructed by incomplete cubane-like units, and that in $[(\text{C}_3\text{H}_8\text{NO})(\text{C}_3\text{H}_7\text{NO})(\text{Cu}_3\text{I}_4)]_n$ is ladder-like motif.

Structure of $(\text{PPh}_3/\text{iPr})_2(\text{Cu}_2\text{I}_4)$ (3**):** **3** has been previously structurally determined, whose planar $(\text{Cu}_2\text{I}_4)^{2-}$ dimer is constructed from two edge-sharing CuI_3 triangles.^[44] The Cu-I lengths and I-Cu-I angles are consistent with those found in other iodocuprates,^[45] and the Cu...Cu distance of 2.9380(11) Å is somewhat longer than reported iodocuprates.^[46] Specially, there are three kinds of C-H... π interactions between adjacent $\text{PPh}_3/\text{iPr}^+$ cations (Table S4). In detail, in each $\text{PPh}_3/\text{iPr}^+$ cation, two phenyl groups involve in C-H... π interactions, upon which a 2-D organic layer is generated. $(\text{Cu}_2\text{I}_4)^{2-}$ dimers fill in the residual interlayers (Figure 2). But no obvious I...I interactions are found between the dimers.

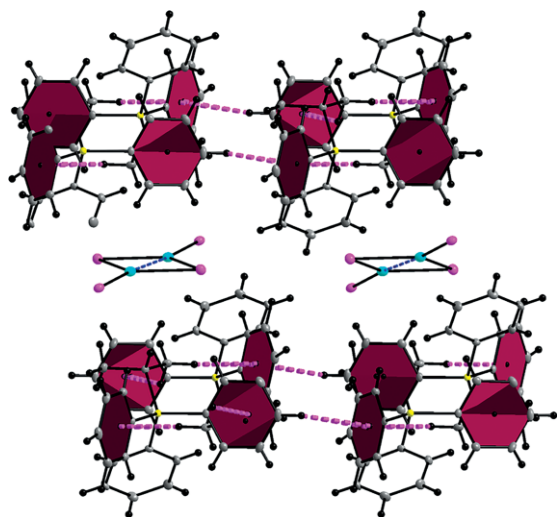


Figure 2. Packing diagram of **3** showing C-H... π interactions.

Water Stability Studies

Up to now, one of the critical drawbacks of photoluminescence (PL) materials is their generally low water stability, which will deter their real applications.^[35] In this work, the alkyl modification on phosphine ligands has been conducted, which might improve their water stability. In the water stability study, the as-synthesized crystalline samples of **1**, **3** and **4** were ground as fine powders and soaked in deionized water at room tempera-

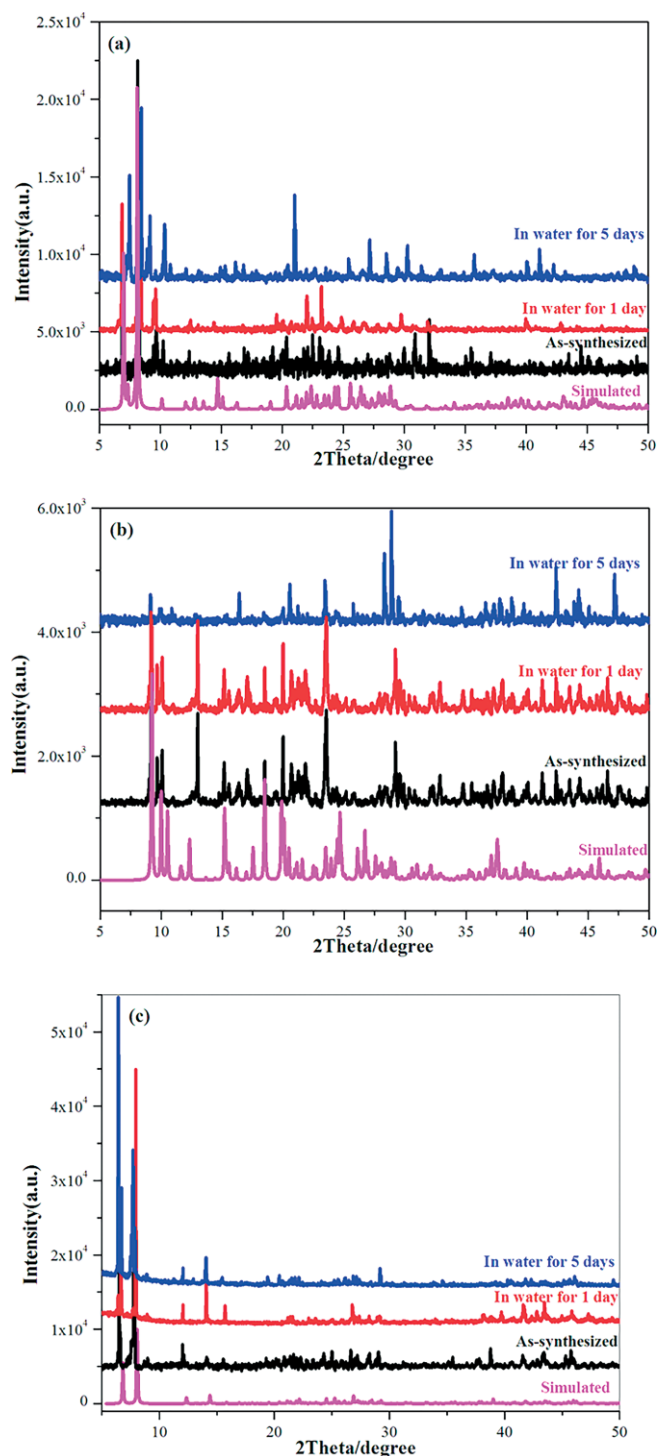
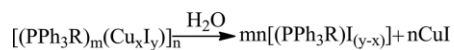


Figure 3. The PXRD patterns of **1** (a), **3** (b) and **4** (c) under different conditions.

ture. Afterwards, the samples were centrifuged and dried at 40 °C at different time intervals. The PXRD experiments were conducted on the collected samples to check their phases.

The phase purities of bulk compounds **1–4** have been verified by powder X-ray diffraction (PXRD). It's obvious that the peaks the experimental patterns are consistent with the corresponding simulated ones, suggesting their good phase purities (Figure 3 and Figure S5). Furthermore, the water stability measurements (Figure 3) imply that the crystal structures of **1**, **3** and **4** can maintain after soaking in water for 1 day. The relatively good water stabilities of these compounds can be assigned to the alkylation of PPh₃ of counteractions, in which both the PPh₃ and the alkyl groups are typical hydrophobic species. Specially, the absence hydrogen-bond donors on quaternary phosphorus salts can rule out the formation of typical strong hydrogen bonds with water in an aqueous system or in moist air, which further improve their water stabilities. However, when extending the soaking time to 5 days, the PXRD patterns of **1** and **3** changed obviously. Compared with the standard pattern of the inorganic structure of CuI (cubic phase, with the space group *F*-43m, and lattice constants *a* = *b* = *c* = 6.04 Å, $\alpha = \beta = \gamma = 90^\circ$, JCPDS No. 77–2391), the samples soaked for 5 days should be the mixtures of bulk crystals and CuI. Their structural collapse might be illustrated as the hydrolysis reactions (Scheme 1).^[13] But **4** is still stable after soaking in 5 days judging from their PXRD. From the above observation, it can be concluded that hybrids **1**, **3** have relatively strong water stabilities, but suffer from hydrolysis reactions after excessive soaking in water. The higher water stability of **4** can be ascribed to the better hydrophobicity of *n*-butyl group, which deters the dispersing of organic and inorganic moieties and as a result, inhibit hydrolysis reaction. In all, introduction of alkyl groups on aromatic molecules is an effective strategy to construct functional hybrid iodocuprates containing positively charged SDAs without introducing strong hydrogen bonding groups. And in the quaternary phosphorus/iodocuprate system, the longer alkyl is, the better water stability can be obtained.



Scheme 1. Possible hydrolysis reactions after excessive soaking in water.

Optical Diffuse-Reflection Spectra

Solid-state optical diffuse-reflection spectra of **1–4** and their corresponding counter-cations were recorded from powder samples at room temperature (Figure 4a). Organic quaternary phosphorus salts and their hybrids **1–4** exhibit intense adsorption in ultraviolet zone (260–450 nm). The adsorption peaks of organic quaternary phosphorus salts appear at about 330 nm, corresponding to the $n-\pi^*/\pi-\pi^*$ transitions of phenyl groups in organic cations. After hybridization with iodocuprates, for **3**, their adsorption peak didn't change, but for **1**, **2** and **4**, the peaks shift to longer waves at about 370 nm. And for all compounds, the absorption bands extend to different extent compared with those of free quaternary phosphorus salts. Because there are no metal-ligand bonds, metal-to-ligand charge trans-

fer (MLCT) transitions and halogen-to-ligand charge transfer (XLCT) can be ruled out. Therefore, the corresponding electronic transitions of **1–4** can definitely assigned to the ligand centred $n-\pi^*/\pi-\pi^*$ transitions of phosphine ligands.^[47] At longer wavelengths over 350 nm, relatively weaker absorption bands are observed, which are not observed for the free ligands. These adsorptions are relevant to ligand-to-ligand charge transfer (LLCT) and charge transfer between inorganic iodocuprates and organic moieties.^[48] The former transitions can be validated by their obvious $\pi-\pi$ and C–H $\cdots\pi$ interactions in their lattices,^[13] and the latter charge transfers have already been reported.^[48]

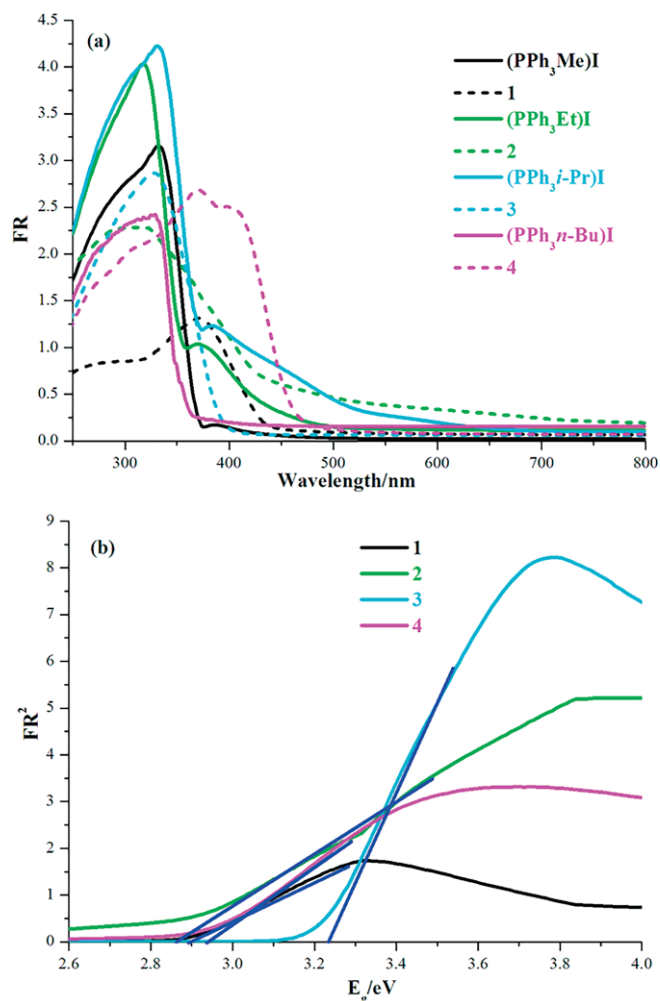


Figure 4. (a) Solid state electronic spectra of **1–4** and their organic counteractions; (b) optical diffuse reflectance spectra for **1–4**.

Solid-state UV/Vis diffuse spectra of **1–4** calculated from the diffuse reflectance data by using the Kubelka–Munk function is plotted in Figure 4b. The band gaps can be estimated as 2.88, 2.86, 3.22 and 2.92 eV for **1–4** respectively, suggesting that all compounds are semi-conductors with broad gaps. Compared with the measured value of 2.95 eV for bulk CuI,^[33] slightly red shifts for **1**, **2** and **4** can be observed, and a 0.27 eV blue-shift occurs in **3**. The shifts reveal obvious intermolecular charge transfer (CT) effect in **1**, **2** and **4**, which are probably led by the strong donating ability of iodocuprate frameworks, rich

π - π interactions, and consequent packing modes.^[49] Noticeably, **1**, **2** and **4** have obviously smaller band gaps than that of **3**, which is in accord with its 0-D cluster structure.

Photophysical Properties

The colors of compound **1-4** under UV, liquid nitrogen are shown in Figure 5. Temperature-dependent luminescences of **1-4** were measured to investigate their response to temperature (Figure 6, Figure 7, Figure 8 and Figure 9). In addition, the

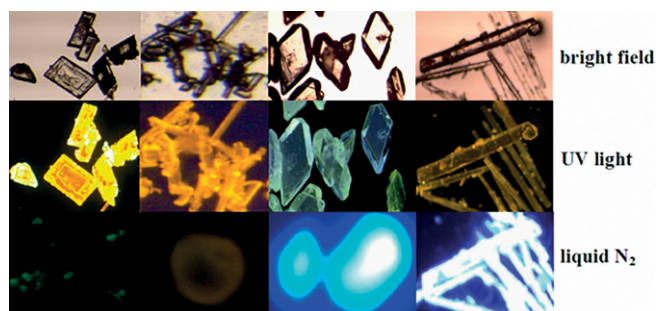


Figure 5. Pictures of **1-4** (from left to right) under different conditions.

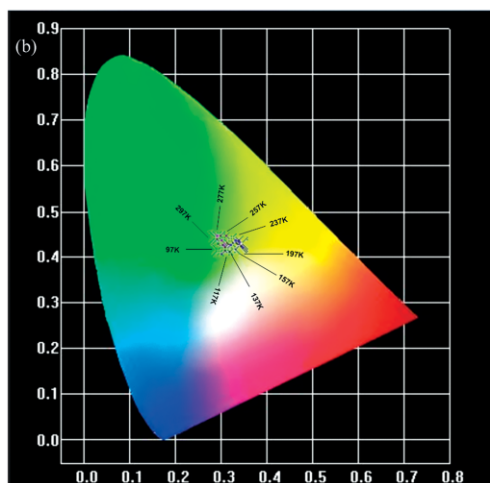
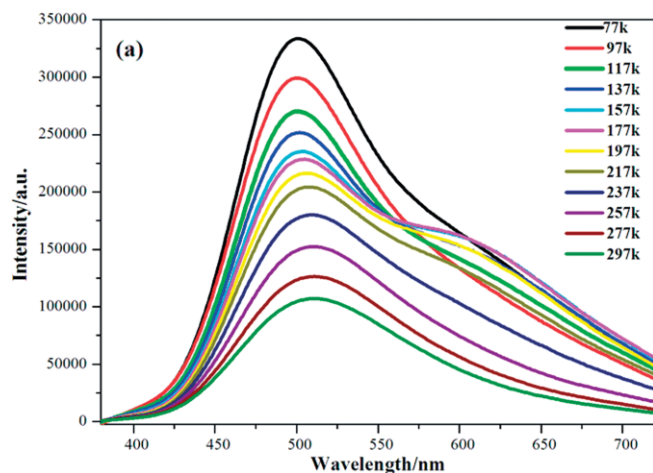


Figure 6. (a) Emission spectra at varied temperatures ($\lambda_{\text{ex}} = 302$ nm) and (b) CIE-1931 chromaticity diagram of **1**.

room temperature luminescence of organic cation (Ph_3PnBu -I was set as example) was measured (Figure S6), and the free organic quaternary phosphorus salt exhibits a strong emission band with a maximum peak around 485 nm under excitation at 340 nm. Compound **1** generates green emission in solid state at room temperature, emitting a single emission band with the maximum peak at about 512 nm ($\lambda_{\text{ex}} = 302$ nm). With the temperature cooled from 297 to 77 K, the intensity of this band increases gradually (Figure 6a). Specially, when temperature was at 197 and 177 K, a new emission at 605 nm appears, but it disappears upon further cooling. And when the sample is gradually warmed up to room temperature, the green emission is back to the initial intensity, illustrating typical reversible luminescent thermochromic behavior. **2** exhibits generally the same reversible luminescent thermochromic behavior with that of **1**, except that the emission is yellow with peak at 592 nm ($\lambda_{\text{ex}} = 373$ nm, Figure 7). **3** and **4** illustrate different temperature-dependent luminescences (Figure 8 and Figure 9). At room temperature, **3** gives a fresh green emission with maximum peak

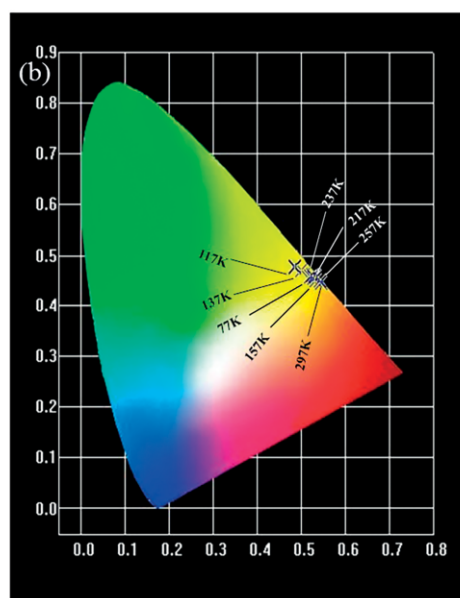
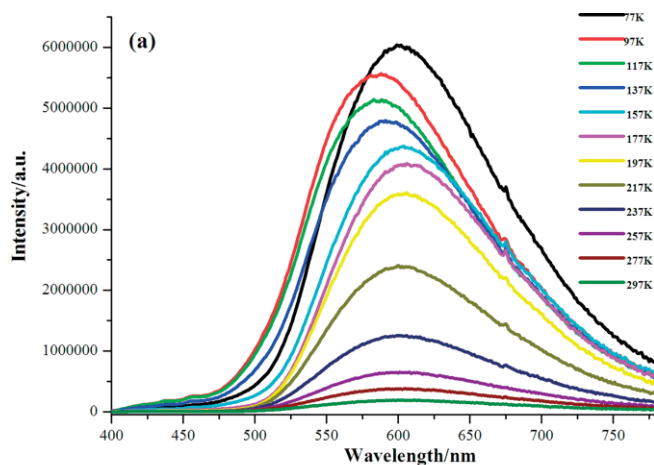


Figure 7. (a) Emission spectra at varied temperatures ($\lambda_{\text{ex}} = 373$ nm) and (b) CIE-1931 chromaticity diagram of **2**.

at about 558 nm [low-energy emission (LE)] at room temperature ($\lambda_{\text{ex}} = 360$ nm). When the temperature is cooled to 237 K, a new blue emission band appears at a higher energy around 447 nm [high-energy emission (HE)]. As further cooling occurs to 77 K, the intensities of these bands increase gradually, but the blue emission is dominated. For **4**, blue and yellow emission (peak at 437, 586 nm, $\lambda_{\text{ex}} = 370$ nm) at room temperature can be observed. When cooled to 177 K, the high-energy blue emission (HE) is greatly intensified and shifts to around 477 nm. As further cooled to 77 K, the intensity of this band increases gradually with the concomitant decreasing of the LE band and a slight blue shift to 460 nm. **3** and **4** also exhibit typical reversible luminescent thermochromic behaviors. Their PL details at room temperature including quantum yields are summarized in Table 1. We can conclude that their colors at low temperature are generally consistent with those in Figure 5. The CIE-1931 emission profiles also show the luminescent color changes of five compounds upon cooling.

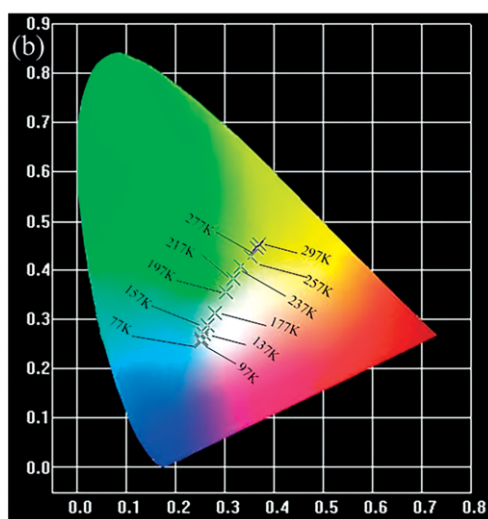
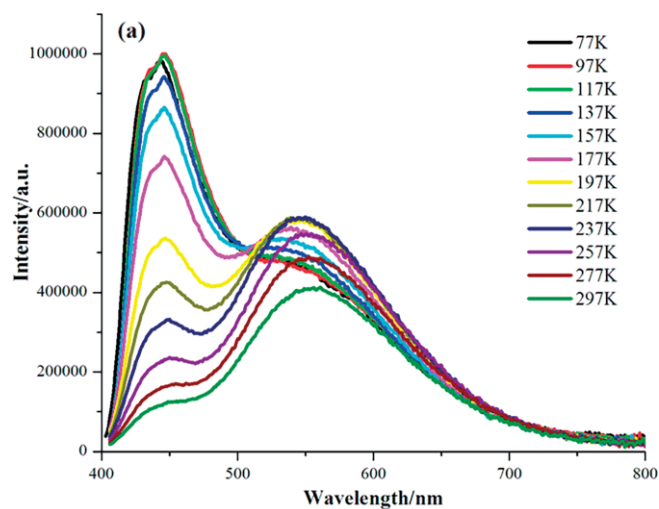


Figure 8. (a) Emission spectra at varied temperatures ($\lambda_{\text{ex}} = 360$ nm) and (b) CIE-1931 chromaticity diagram of **3**.

About the photophysical properties of iodocuprate(I)-based hybrids, great efforts have been devoted to the iodocuprate-

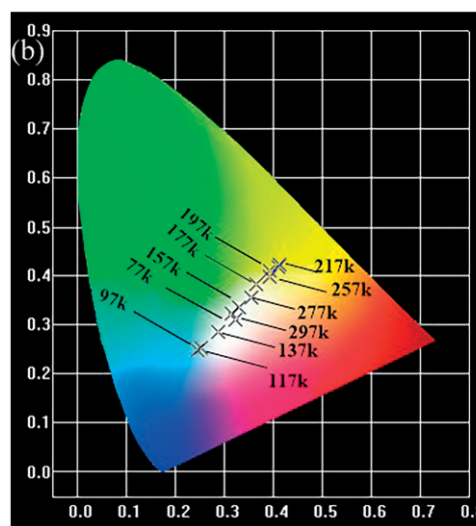
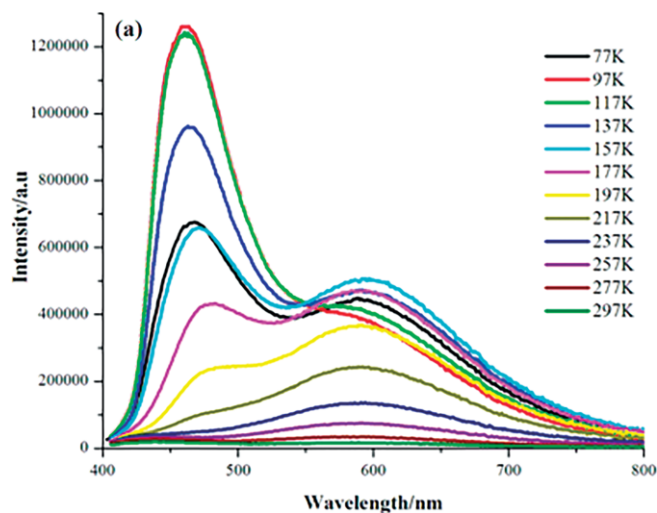


Figure 9. (a) Emission spectra at varied temperatures ($\lambda_{\text{ex}} = 370$ nm) and (b) CIE-1931 chromaticity diagram of **4**.

Table 1. PL data of compound **1–4** at room temperature.

Compound	λ_{ex} [nm]	λ_{em} [nm]	Φ [%]
1	302	512	6.55
2	373	602	6.29
3	360	558	6.22
4	370	437/586	6.19

based coordinated polymers,^[50,51] but much less attention was paid to the iodocuprate/SDA system.^[14] In the former case, two emission bands (LE and HE) can be seen in the temperature-dependent luminescences, in which the LE bands are attributed to the iodocuprate cluster-centered CT (ICCT) excited state and the HE bands to an iodide to phosphine ligand charge transfer (XLCT).^[50,52] In the iodocuprate cluster-centered (ICCT) process, Cu–Cu distances were changed as the temperature cooling, leading to geometrical variations of iodocuprate clusters.^[53] In the iodocuprate/SDA system, the strong and broad single-band emissions can also be assigned to iodocuprate moieties without the presence of organic counterions.^[14] Based on these liter-

atures and the emission of free counteraction ($\text{Ph}_3\text{PnBu}\cdot\text{I}$, Figure S6), the LE emissions of **1–4** stem from the iodocuprate moieties, and the HE emissions of **3** and **4** are the contribution of ligand-centered transitions (LLCT). Iodide to phosphine ligand charge transfer (XLCT) can be ruled out due to longer I...P distances (longer than 5.1 Å). In addition, the temperature stimulus can lead to the configuration change of iodocuprate moieties, and furthermore, affect the frontier molecular orbitals.^[53] According to structural analysis, the Cu–Cu distances are elongated to some extent when substituent lengths increase. Generally, the more relaxed iodocuprates will be more sensitive to thermal stimulus. Therefore, from methyl to *n*-butyl substituents, red-shift can be observed for **1**, **2** and **4**. It's interesting that no HE emissions can be found in **1** and **2**, we can explain that the stacking modes of organic counteractions with strong π – π stacking interactions quench these emissions. Besides, for **1**, the appearance of new emission band of 605 nm at 197 and 177 K might be attributed to promoted structural torsion at these temperatures and increased localization of the excited state.^[54] For **3**, no HE emissions can be detected at room temperature, but such blue emission appears in **4**. This might be led by stronger C–H... π interaction in **4**, which enhance the ligand-to-ligand transition. Judging from this trend, we can tune the luminescences of this kind of compounds by introducing different substituents on Ph_3P , which has never been studied in iodocuprate(I)-based hybrids.

Photocurrent Response Properties

Photocurrent generation has been observed in metal halide based hybrids.^[55,56] Photoelectrochemical experiments have also been performed on **1**, **3** and **4** according to typical method. The SEM diagrams of films coated with **1**, **3** and **4** are shown in Figure S7. In detail, three electrode photo/electrochemical cell system was adopted (sample modified ITO electrode, a Pt wire as auxiliary electrode and a Ag/AgCl electrode as reference electrode). The photocurrent response behaviors in Na_2SO_4 aqueous solution under the illumination from a 150 W Xe arc lamp with on–off cycles are shown in Figure 10. The results show that under the repetitive irradiation (the on–off interval of 10 s), repeatable and steady photocurrents with rapid responses can be detected. Specially, the photocurrent of **1** decreases to some extent firstly but stabilizes after five cycles. On the contrary, **4** increases gradually and stabilizes after four cycles. The photocurrents of **1**, **3** and **4** all stabilize at about 4.40×10^{-7} , 4.55×10^{-7} and 4.75×10^{-7} A, respectively. The current intensities of this work are weaker than the other viologen-containing compounds, such as $(\text{MV})_2[\text{Li}_4(\text{L})_2(\text{H}_2\text{O})_6]$ and $\text{MV}[\text{Ni}(4\text{-pedt})_2]_2$,^[57] but stronger than metallohydrogen-containing hybrids.^[55] It has been proved that that the pure organic-coated sole system shows no photocurrent response,^[58] therefore, in this work, iodocuprate–quaternary phosphorus donor–acceptor systems are the reason for photocurrent generation. Judging from this fact, the photocurrent generation mechanism can be proposed: upon irradiation, the photosensitive quaternary phosphorus cations are excited to generate the Ph_3PR^+ radicals, at the same time, $\text{Cu}_x\text{I}_y^{(y-x)-}$ donors can also provide

electrons to quaternary phosphorus moieties. Secondly, the Ph_3PR^+ radicals transfer their electrons to the ITO electrodes with re-production of Ph_3PR^+ acceptor. The $\text{Cu}_x\text{I}_y^{(y-x)-}$ anions lose one electron to generate the $\text{Cu}_x\text{I}_y^{(y-x)-\cdot}$ radicals to produce the electron conductive pair of $\text{Cu}_x\text{I}_y^{(y-x)-}\text{-Ph}_3\text{PR}^+$. This process can also be verified by components of top of VBs (Cu-3d, I-5p) and the bottom of CBs (p - π^* anti-bonding orbital of the quaternary phosphorus) in PDOS (Figure 11 and Figure S8). According to this mechanism, the more electronic rich in $\text{Cu}_x\text{I}_y^{(y-x)-}$ donors can facilitate the electronic transfer. Therefore, $(\text{Cu}_2\text{I}_4)^{2-}$ of **3** is more electronic rich than $(\text{Cu}_3\text{I}_4)^-$ chain in **1** and **4**, which gives rise to a relative higher current intensity in **3**.

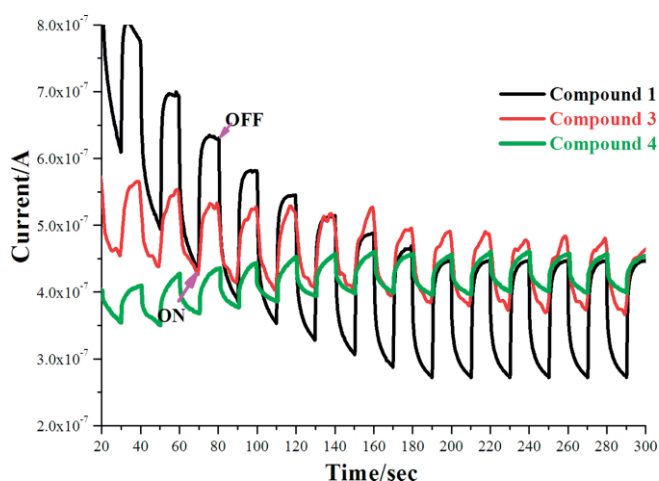


Figure 10. Photocurrent response behaviors in this work.

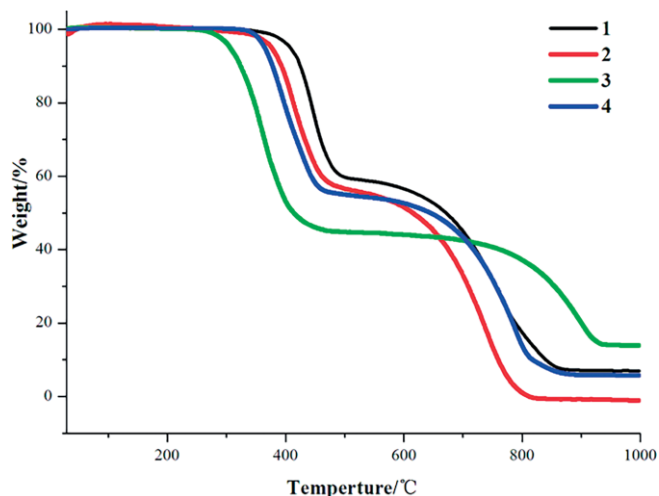


Figure 11. Thermogravimetric analysis (TGA) traces for 1–4.

Thermoanalytical Properties

To examine the thermal stabilities of **1–4**, TGA were carried out in the temperature range of 30–1000 °C with a rate of 10 °C min^{-1} under Ar_2 gas, the results of which are presented in Figure 11. **1–4** exhibit similar weight loss trends, in which two steps weight loss can be observed. The first occurred at

280–500 °C (for **1**: weight loss 41.81 %, theoretical value 41.43 %; for **2**: weight loss 42.62 %, theoretical value 42.473 %; for **4**: weight loss 44.09 %, theoretical value 43.56 %), which are due to the loss of organic $\text{PPh}_3\text{R}\cdot\text{I}$ quaternary phosphorus salts. But **3** is different from others, which loses its $(\text{PPh}_3/\text{Pr})^+$ cation in this stage (experimental 49.04 vs. theoretical 53.22 %). In the second stage occurring among 640–930 °C, the iodocuprates collapse with sublimed I_2 dissociated from skeletons. In all, all compounds exhibit good thermal stabilities with decomposition temperature ranging among 280–350 °C. Comparably, thermal stabilities of **1**, **2**, **4** are higher than that of **3**, which is consistent with their structural features.

Electronic Structure and Photophysical Property Mechanisms

To look further insight into the optical properties of **1–4**, theoretical studies including the band structure along with high symmetry points of the first Brillouin zone, and density of states (DOS) were performed using the CASTEP code in Materials Studio 8.0. The X-ray crystallographic data were used to construct the calculated modes without optimization. The bands can be assigned according to total and partial densities of states (PDOS, Figure 12 and Figure S8). As shown by the total and partial DOS diagrams, they possess similar electronic structures. In detail, the top of the VBs between -5 and 0 eV are mainly from the contributions of the π bonding orbitals of organic cation, I-5p state and Cu-3d state, but I-5p/Cu-3d are dominated at around the Fermi level. The bottom of the CBs between 0 and 5 eV are mainly from the contribution of the p - π^* antibonding orbital of the quaternary phosphorus SDAs, and Cu-4p, I-5s/5p also gives small amount of contribution. In the band gap engineering of organic/metal halide system, it is universally accepted that the band gap adjustments of inorganic metal halides can be realized by the insertion of molecular orbitals of organic cations into the empty band of parent metal halides.^[59,60] This trend can also be seen in this work. Accordingly, the intrinsic absorption of **1–4** can be mainly ascribed to

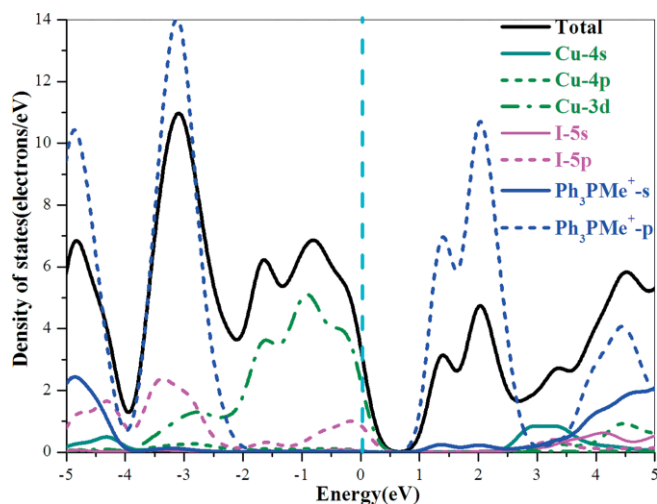


Figure 12. Total and partial density of states of **1**.

the charge transitions between organic SDAs accompanied by charge transfer between inorganic-organic species. In addition, the components of CBs and VBs suggest the multiple energy transfer processes in their PL behavior, i.e., iodocuprate cluster-centered CT (ICCT) and ligand-to-ligand charge transfer (LLCT). These calculated results are in agreement with the PL assignments of **1–4**. Besides, these electronic structures support the photocurrent generation mechanism.

Conclusions

In summary, iodocuprates(I) hybrids directed by alkylated (triphenyl)phosphonium have been prepared. With the lengthening of alkyl groups on P-atom, the weakened $\text{Cu}\cdots\text{Cu}$ and π - π stacking interactions were observed, which are relative to their water stabilities and luminescent thermochromic behaviors. Besides, effective and repeatable photocurrent responses can be detected. In all, employing alkylated (triphenyl)phosphonium as SDAs to prepare hybrid iodocuprates is an effective approach to obtain strong PL materials with enhanced water stability. This strategy will be beneficial for the rational design and synthesis of iodocuprate-based PL materials with higher performance. The work about introduction of other functional groups on substituted alkyls as SDAs is still ongoing.

Experimental Section

Materials and Instruments: All chemicals except quaternary phosphorus salts were commercial products and used without further purification. IR spectra were recorded on a Perkin–Elmer Spectrum-2000 FTIR spectrophotometer (4000 – 400 cm^{-1}) on powdered sample spread on KBr plate. Elemental analyses for C, H and N were performed on a Vario MICRO elemental analyzer. Optical diffuse reflectance spectra were measured on a Perkin–Elmer lambda 900 UV/Vis spectrophotometer equipped with an integrating sphere at 293 K, and BaSO_4 plates were used as reference. Powder XRD patterns were obtained using a Philips X'Pert-MPD diffractometer with $\text{Cu-K}\alpha$ radiation ($\lambda = 1.54056$ Å). Fluorescence spectra were carried out on an Edinburgh FL-FS 920 TCSPC spectrometer. The luminescence quantum yields were recorded on a Hamamatsu Photonics C11347–11 absolute photoluminescence quantum yield spectrometer. ^1H NMR spectra were recorded on a Bruker Avance III 400 MHz NMR spectrometer. The morphologies of electrodes with films of **1**, **3** and **4** were observed by using a HIROX SH-4000 energy spectrometer. The photocurrent experiments were performed on a CHI650 electrochemistry workstation with three-electrode systems. TGA for **1–4** were carried out under argon atmosphere in the range of 30 – 1000 °C with a scan rate of 10 °C min^{-1} using a NETZSCH STA449F5 Jupiter thermogravimetric analyzer.

Single Crystal X-ray Diffraction Analyses: The intensity data of **1–4** were collected on a Bruker APEX II diffractometer using graphite-monochromated $\text{MoK}\alpha$ radiation ($\lambda = 0.71073$ Å) at room temperature, during which the L_p factor corrections and multi-scan absorption corrections were applied. The structure was solved by direct methods with SHELX-97 program and refined by full-matrix least-squares techniques on F^2 with SHELXL-97 program.^[61,62] For all non-hydrogen atoms, anisotropic refinements were carried out. All hydrogen atoms attached to carbon atoms were geometrically placed. Crystal parameters of four compounds were summarized in

Table 2. Summary of the crystal data and structure determination for **1–4**.

Compound	1	2	3	4
Empirical formula	C ₁₉ H ₁₈ Cu ₃ I ₄ P	C ₂₀ H ₂₀ Cu ₃ I ₄ P	C ₂₁ H ₂₂ Cu ₂ P	C ₂₂ H ₂₄ Cu ₃ I ₄ P
Formula mass	975.55	989.58	622.71	1017.63
Crystal system	Monoclinic	Monoclinic	Monoclinic	Orthorhombic
Space group	<i>P</i> 2 ₁ / <i>c</i>	<i>P</i> 2 ₁ / <i>c</i>	<i>P</i> 2 ₁ / <i>n</i>	<i>Pbca</i>
<i>a</i> [Å]	12.6129(16)	12.8246(11)	11.5661(4)	8.0261(5)
<i>b</i> [Å]	25.241(3)	25.251(2)	12.2769(4)	25.1831(16)
<i>c</i> [Å]	8.0055(10)	8.0659(7)	15.2877(6)	27.2628(17)
β [°]	107.327(2)	106.683(2)	94.788(4)	90.00
<i>V</i> [Å ³]	2433.0(5)	2502.1(4)	2163.21(13)	5510.4(6)
<i>Z</i>	4	4	4	8
<i>D_c</i> [g/cm ³]	2.663	2.627	1.912	2.453
μ [mm ⁻¹]	7.743	7.532	3.940	6.843
<i>F</i> (000)	1784	1816	1192	3760
Reflections, total	8055	8020	11314	35863
Reflections, unique	4253 (<i>R</i> _{int} = 0.0234)	4299 (<i>R</i> _{int} = 0.0272)	3591 (<i>R</i> _{int} = 0.0157)	4855 (<i>R</i> _{int} = 0.0522)
Reflections, observed	3516	3269	3364	3640
Goodness-of-fit on <i>F</i> ²	1.081	1.020	1.367	1.087
No. of parameters refined	245	333	292	271
<i>R</i> [<i>I</i> > 2 σ (<i>I</i>)]	0.0363	0.0391	0.0196	0.0351
<i>R_w</i> [<i>I</i> > 2 σ (<i>I</i>)]	0.0785	0.0765	0.0749	0.0913
Residual extremes [e/Å ³]	0.883, -1.295	0.900, -1.344	0.653, -1.172	1.328, -1.710

Table 2. Selected bond lengths and angles are listed in Table S1–S2, π – π stacking interactions and C–H \cdots π interactions are given in Table S3 and S4.

CCDC 1818467 (for **1**), 1590153 (for **2**), 1815248 (for **3**), and 1812547 (for **4**) contain the supplementary crystallographic data for this paper. These data can be obtained free of charge from The Cambridge Crystallographic Data Centre.

Electrode Preparation and Photocurrent Measurement: Typical solution coating method is utilized to prepare the photocurrent measurement electrodes of compounds **1**, **3** and **4**.^[63] 5 mg as-synthesized powder was dissolved in 0.3 mL of DMF, and the suspension was dispersed evenly to obtain a slurry. The slurry was spread onto pre-cleaned ITO glass (0.6 × 0.6 cm, 14 Ω per cm²), whose side part was previously protected using scotch tape. The working electrode was dried overnight under ambient conditions. A copper wire was connected to the side part of the working electrode using conductive tape. Uncoated parts of the electrode were isolated with epoxy resin. A 150 W high-pressure xenon lamp, located 15 cm away from the surface of the ITO electrode, was employed as a full-wavelength light source. The photocurrent experiments were performed on a CHI660 electrochemistry workstation in a three-electrode system, with the sample-coated ITO glass as the working electrode mounted on the window with an area of 0.25 cm², a Pt wire as auxiliary electrode, and a Ag/AgCl electrode as reference electrode. The supporting electrolyte solution was a 0.2 mol L⁻¹ sodium sulfate aqueous solution. The applied potential was 0.5 V for all measurements. The lamp was kept on continuously, and a manual shutter was used to block exposure of the sample to the light. The sample was typically irradiated at intervals of 10 s.

Computational Details: The cif files of **1–3** were used to construct the calculated models. The electronic structure calculations were carried out using density functional theory (DFT) with the three non-local gradient-corrected exchange–correlation functions (GGA-PBE) and using CASTEP code,^[64] which uses a plane wave basis set for the valence electrons and norm-conserving pseudopotential for the core electrons. The number of plane waves included in the basis was determined by a cutoff energy *E_c* of 550 eV. The parameters used in the calculations and convergence criteria were according to the default values of the CASTEP program in Materials Studio 8.0.

Synthesis

Synthesis of Quaternary Phosphorus Salts: Quaternary phosphorus salts were prepared by one step alkylated reaction of triphenylphosphine with iodomethane, iodoethane, isopropane iodide, *n*-butyl iodide in the toluene solvent according to literature method.^[65,66] The detail synthesis process, ¹H NMR spectra of four quaternary phosphorus salts can be seen in Figure S2 (electronic supplementary material).

Synthesis of [(PPh₃Me)(Cu₃I₄)]_{*n*} (1**):** Compound **1** was prepared by solution evaporation method. PPh₃Me·I (0.0808 g, 0.2 mmol) and CuI (0.0190 g, 0.1 mmol) were dissolved in 45 mL of ethanol, and kept stirring at 45 °C for 2 h. The obtained solution was filtered, and red filtrate liquor was covered with a cling film at room temperature for slow evaporation. Colorless transparent lumpy crystals were obtained after the growth period of 3 d. Yield: 76.3 % (0.0248 g, based on Cu). C₁₉H₁₈Cu₃I₄P (975.55): calcd. C 23.39, H 1.86; found C 23.75, H 1.72. IR: $\tilde{\nu}$ = 3070 (w), 1579 (w), 1479 (s), 1422 (s), 1316 (w), 1181 (m), 1160 (m), 1096 (s), 1075 (m), 1003 (w), 748 (s), 691 (s), 613 (w), 485 (s) cm⁻¹.

Synthesis of [(PPh₃Et)(Cu₃I₄)]_{*n*} (2**):** The synthesis process of **2** is similar to that of **1**, expect PPh₃Et·I (0.0836 g, 0.2 mmol) was used as starting material. Colorless transparent block crystals were obtained after 3 d. Yield: 63.2 % (0.0209 g, based on Cu). C₂₀H₂₀Cu₃I₄P (989.58): calcd. C 23.39, H 1.86; found C 23.75, H 1.72. IR: $\tilde{\nu}$ = 3090 (w), 2920 (m), 1584 (w), 1492 (s), 1487 (s), 1403 (m), 1235 (w), 1185 (m), 1190 (s), 998 (s), 769 (s), 726 (s), 495 (s), 454 (s) cm⁻¹.

Synthesis of [(PPh₃iPr)₂(Cu₂I₄)]_{*n*} (3**):** The synthesis process of **3** is also similar to that of **1**, expect PPh₃iPr·I (0.0864 g, 0.2 mmol) and CuI (0.0380 g, 0.2 mmol) were used as starting materials. Colorless transparent block crystals with yield of 54.6 % (0.0680 g based on Cu) were obtained. C₂₁H₂₂Cu₂P (622.71): calcd. C 40.50, H 3.56; found C 41.05, H 3.32. IR: $\tilde{\nu}$ = 3080 (w), 2932 (m), 1584 (w), 1480 (s), 1482 (s), 1378 (m), 1220 (w), 1146 (m), 1198 (s), 872 (s), 724 (s), 492 (s), 409 (m) cm⁻¹.

Synthesis of [(PPh₃*n*Bu)(Cu₃I₄)]_{*n*} (4**):** Compound **4** was synthesized using the same condition with that of **1**, in which PPh₃*n*Bu·I (0.0651 g, 0.1 mmol) and CuI (0.0190 g, 0.1 mmol) were used as starting materials. Colorless transparent lumpy crystals with yield of

61.3 % (0.0208 g based on Cu) were obtained. The SEM diagrams of **1–4** can be seen in the Figure S1 in ESI. Specially, the morphology of **4** is different from others due to its orthorhombic system with higher symmetry (other compounds are monoclinic systems). $C_{22}H_{24}Cu_3I_4P$ (1017.63): calcd. C 25.94, H 2.38; found C 25.65, H 2.29. IR: $\tilde{\nu} = 3032$ (w), 2932 (m), 1567 (m), 1480 (w), 1459 (s), 1380 (m), 1314 (w), 1192 (m), 1197 (s), 997 (s), 897 (s), 789 (s), 716 (s), 690 (s), 495 (s), 412 (m) cm^{-1} .

Supporting Information (see footnote on the first page of this article): The synthesis details of organic quaternary phosphorus salts, the selected bond lengths and angles, hydrogen bond details, π - π stacking interactions, C-H $\cdots\pi$ interaction parameters, SEM diagrams, NMR spectra of quaternary phosphorus salts, additional structural figures PXRD patterns, solid luminescence of PPH_3nBu -I, SEM images of films, total and partial density of states are available.

Acknowledgments

We acknowledge support of this research by National Natural Science Foundation of China (NOS: 21771038) and National Natural Science Foundation of Fujian Province (2018J01684, 2017J01409).

Keywords: Iodocuprate · Quaternary Phosphorus · Luminescence · Photocurrent Response

- [1] K. T. Kamtekar, A. P. Monkman, M. R. Bryce, *Adv. Mater.* **2010**, *22*, 572–582.
- [2] V. Fernandez-Moreira, F. L. Thorp-Greenwood, M. P. Coogan, *Chem. Commun.* **2010**, *46*, 186–202.
- [3] R. Peng, M. Li, D. Li, *Coord. Chem. Rev.* **2010**, *254*, 1–18.
- [4] M. Wallesch, D. Volz, D. M. Zink, U. Schepers, M. Nieger, T. Baumann, S. Brase, *Chem. Eur. J.* **2014**, *20*, 6578–6590.
- [5] W. Liu, Y. Fang, G. Z. Wei, S. J. Teat, K. C. Xiong, Z. C. Hu, W. P. Lustig, J. Li, *J. Am. Chem. Soc.* **2015**, *137*, 9400–9408.
- [6] K. Tsuge, Y. Chishina, H. Hashiguchi, Y. Sasaki, M. Kato, S. Ishizaka, N. Kitamura, *Coord. Chem. Rev.* **2016**, *306*, 636–651.
- [7] X. C. Shan, F. L. Jiang, D. Q. Yuan, H. B. Zhang, M. Y. Wu, L. Chen, J. Wei, S. Q. Zhang, J. Pan, M. C. Hong, *Chem. Sci.* **2013**, *4*, 1484–1489.
- [8] C. Tard, S. Perruchas, S. Maron, X. F. Le Goff, F. Guillen, A. Garcia, J. Vigneron, A. Etcheberry, T. Gacoin, J. P. Boilot, *Chem. Mater.* **2008**, *20*, 7010–7016.
- [9] S. Perruchas, X. F. LeGoff, S. Maron, I. Maurin, F. Guillen, A. Garcia, T. Gacoin, J. P. Boilot, *J. Am. Chem. Soc.* **2010**, *132*, 10967–10969.
- [10] Q. Benito, X. F. Le Goff, S. Maron, A. Fargues, A. Garcia, C. Martineau, F. Taulelle, S. Kahlal, T. Gacoin, J. P. Boilot, S. Perruchas, *J. Am. Chem. Soc.* **2014**, *136*, 11311–11320.
- [11] X. Zhang, W. Liu, G. Z. Wei, D. Banerjee, Z. Hu, J. Li, *J. Am. Chem. Soc.* **2014**, *136*, 14230–14236.
- [12] J. J. Shen, X. X. Li, T. L. Yu, F. Wang, P. F. Hao, Y. L. Fu, *Inorg. Chem.* **2016**, *55*, 8271–8273.
- [13] G. N. Liu, R. Y. Zhao, H. Xu, Z. H. Wang, Q. S. Liu, M. Z. Shahid, J. L. Miao, G. Chen, C. Li, *Dalton Trans.* **2018**, *47*, 2306–2317.
- [14] E. Jalilian, R. Z. Liao, F. Himo, H. Brismar, F. Laurell, S. Lidin, *CrystEngComm* **2011**, *13*, 4729–4734.
- [15] E. Cariati, E. Lucentib, C. Bottad, U. Giovanellad, D. Marinottoc, S. Righettoa, *Coord. Chem. Rev.* **2016**, *306*, 566–614.
- [16] R. Peng, M. Li, D. Li, *Coord. Chem. Rev.* **2010**, *254*, 1–18.
- [17] P. C. Ford, E. Cariati, J. Bourassa, *Chem. Rev.* **1999**, *99*, 3625–3647.
- [18] V. W. W. Yam, K. M. C. Wong, *Chem. Commun.* **2011**, *47*, 11579–11592.
- [19] K. Tsuge, Y. Chishina, H. Hashiguchi, Y. Sasaki, M. Kato, S. Ishizaka, N. Kitamura, *Coord. Chem. Rev.* **2016**, *306*, 636–651.
- [20] M. Sebastian, J. L. Markus, Y. Hartmut, P. Arno, *Dalton Trans.* **2015**, *44*, 19305–19313.
- [21] E. Jalilian, S. Lidin, *CrystEngComm* **2011**, *13*, 5730–5736.
- [22] R. Farra, K. Thiel, A. Winter, T. Klamroth, A. Poppl, A. Kelling, U. Schilde, A. Taubert, P. Strauch, *New J. Chem.* **2011**, *35*, 2793–2803.
- [23] E. C. Hosten, R. Betz, *Z. Kristallogr. New Cryst. Struct.* **2016**, *231*, 355.
- [24] E. Jalilian, R. Z. Liao, F. Himo, H. Brismar, F. Laurell, S. Lidin, *CrystEngComm* **2011**, *13*, 4729–4734.
- [25] H. Hartl, F. Mahdjour-Hassan-Abadi, *Angew. Chem. Int. Ed. Engl.* **1994**, *33*, 1841–1842; *Angew. Chem.* **1994**, *106*, 1929.
- [26] A. Pfitzner, D. Schmitz, *Z. Anorg. Allg. Chem.* **1997**, *623*, 1555–1560.
- [27] H. Hartl, F. Mahdjour-Hassan-Abadi, *Z. Naturforsch. B* **1984**, *39*, 149–156.
- [28] G. A. Bowmaker, G. R. Clark, D. K. P. Yuen, *J. Chem. Soc., Dalton Trans.* **1976**, 2329–2334.
- [29] G. A. Bowmaker, G. R. Clark, D. A. Rogers, *J. Chem. Soc., Dalton Trans.* **1984**, 37–45.
- [30] S. Ramaprabhu, R. Ferretti, E. A. C. Lucken, G. Bernardinelli, *Inorg. Chim. Acta* **1994**, *227*, 153–157.
- [31] G. A. Bowmaker, M. I. Bruce, B. W. Skelton, N. Somers, A. H. White, *Z. Anorg. Allg. Chem.* **2007**, *633*, 1024–1030.
- [32] M. Hashimoto, S. Igawa, M. Yashima, I. Kawata, M. Hoshino, M. Osawa, *J. Am. Chem. Soc.* **2011**, *133*, 10348–10351.
- [33] Q. Zhang, T. Komino, S. Huang, S. Matsunami, K. Goushi, C. Adachi, *Adv. Funct. Mater.* **2012**, *22*, 2327–2336.
- [34] X. L. Chen, R. M. Yu, Q. K. Zhang, L. J. Zhou, X. Y. Wu, Q. Zhang, C. Z. Lu, *Chem. Mater.* **2013**, *25*, 3910–3920.
- [35] W. Liu, K. Zhu, S. J. Teat, G. Dey, Z. Q. Shen, L. Wang, D. M. O'Carroll, J. Li, *J. Am. Chem. Soc.* **2017**, *139*, 9281–9290.
- [36] X. W. Lei, C. Y. Yue, J. Q. Zhao, Y. F. Han, J. T. Yang, R. R. Meng, C. S. Gao, H. Ding, C. Y. Wang, W. D. Chen, *Cryst. Growth Des.* **2015**, *15*, 5416–5426.
- [37] J. J. Hou, S. L. Li, C. R. Li, X. M. Zhang, *Dalton Trans.* **2010**, *39*, 2701–2707.
- [38] Y. R. Qiao, P. Hao, Y. Fu, *Inorg. Chem.* **2015**, *54*, 8705–8710.
- [39] J. K. Cheng, Y. G. Yao, J. Zhang, Z. J. Li, Z. W. Cai, X. Y. Zhang, Z. N. Chen, Y. B. Chen, Y. Kang, Y. Y. Qin, Y. H. Wen, *J. Am. Chem. Soc.* **2004**, *126*, 7796–7797.
- [40] H. H. Li, Z. R. Chen, J. Q. Li, H. B. Zhan, W. X. Zhang, C. C. Huang, C. Ma, B. Zhao, *J. Solid State Chem.* **2006**, *179*, 1415–1420.
- [41] A. B. Corradi, M. R. Cramarossa, T. Manfredini, L. P. Battaglia, G. Pelosi, A. Saccani, F. Sandrolini, *J. Chem. Soc., Dalton Trans.* **1993**, 3587–3591.
- [42] H. Hartl, F. Mahdjour-Hassan-Abadi, *Angew. Chem. Int. Ed. Engl.* **1994**, *33*, 1841–1842; *Angew. Chem.* **1994**, *106*, 1929.
- [43] N. P. Rath, E. M. Holt, *J. Chem. Soc., Chem. Commun.* **1985**, *10*, 665–667.
- [44] E. Jalilian, S. Lidin, *Acta Crystallogr., Sect. E* **2010**, *66*, m432–m433.
- [45] E. Cariati, R. Macchi, D. Roberto, R. Ugo, S. Galli, N. Masciocchi, A. Sironi, *Chem. Mater.* **2007**, *19*, 3704–3711.
- [46] Y. F. Liu, J. Z. Chen, C. C. Huang, *Acta Crystallogr., Sect. E* **2007**, *63*, m2957–m2965.
- [47] C. H. Huang, M. Wen, C. Y. Wang, Y. F. Lu, X. H. Huang, H. H. Li, S. T. Wu, N. F. Zhuang, X. L. Hu, *Dalton Trans.* **2017**, *46*, 1413–1419.
- [48] L. J. Xu, J. Y. Wang, X. F. Zhu, X. C. Zeng, Z. N. Chen, *Adv. Funct. Mater.* **2015**, *25*, 3033–3042.
- [49] T. L. Yu, J. J. Shen, Y. L. Wang, Y. L. Fu, *Eur. J. Inorg. Chem.* **2015**, 1989–1996.
- [50] X. C. Shan, H. B. Zhang, L. Chen, M. Y. Wu, F. L. Jiang, M. C. Hong, *Cryst. Growth Des.* **2013**, *13*, 1377–1381.
- [51] X. C. Shan, F. L. Jiang, L. Chen, M. Y. Wu, J. Pan, X. Y. Wan, M. C. Hong, *J. Mater. Chem. C* **2013**, *1*, 4339–4349.
- [52] Z. Liu, P. I. Djurovich, M. T. Whited, M. E. Thompson, *Inorg. Chem.* **2012**, *51*, 230–236.
- [53] T. H. Kim, Y. W. Shin, J. H. Jung, J. S. Kim, J. Kim, *Angew. Chem. Int. Ed.* **2008**, *47*, 685–688; *Angew. Chem.* **2008**, *120*, 697.
- [54] M. J. Leilt, V. A. Krylova, P. I. Djurovich, M. E. Thompson, H. Yersin, *J. Am. Chem. Soc.* **2014**, *136*, 16032–16038.
- [55] D. H. Wang, L. M. Zhao, X. Y. Lin, Y. K. Wang, W. T. Zhang, K. Y. Song, H. H. Li, Z. R. Chen, *Inorg. Chem. Front.* **2018**, *5*, 1162–1173.
- [56] L. M. Zhao, W. T. Zhang, K. Y. Song, Q. Q. Wu, Y. Li, H. H. Li, Z. R. Chen, *CrystEngComm* **2018**, *20*, 2245–2252.
- [57] Y. D. Huang, P. Huo, M. Y. Shao, J. X. Yin, W. C. Shen, Q. Y. Zhu, J. Dai, *Inorg. Chem.* **2014**, *53*, 3480–3487.
- [58] W. C. Shen, P. Huo, Y. D. Huang, J. X. Yin, Q. Y. Zhu, J. Dai, *RSC Adv.* **2014**, *4*, 60221–60226.
- [59] H. H. Li, J. X. Wu, H. J. Dong, Y. L. Wu, Z. R. Chen, *J. Mol. Struct.* **2011**, *987*, 180–185.

- [60] C. Sun, M. S. Wang, X. Zhang, N. N. Zhang, L. R. Cai, G. C. Guo, *CrystEng-Comm* **2017**, *19*, 4476–4479.
- [61] G. M. Sheldrick, *SHELXS-97: Program for Crystal Structure Solution*; Göttingen University: Göttingen, Germany, **1997**.
- [62] G. M. Sheldrick, *SHELXL-97: Program for the Refinement of Crystal Structures*; Göttingen University: Göttingen, Germany, **1997**.
- [63] J. L. Hou, W. Luo, Y. Guo, P. Zhang, S. Yang, Q. Y. Zhu, J. Dai, *Inorg. Chem.* **2017**, *56*, 6451–6458.
- [64] M. Segall, P. Lindan, M. Probert and C. Pickard, et al., *Materials Studio CASTEP version 8.0*, **2012**.
- [65] Y. Zhao, T. Feng, G. Li, F. Liu, X. Dai, Z. Dong, X. Qiu, *RSC Adv.* **2016**, *6*, 42482–42494.
- [66] Y. Uchiyama, T. Ohtsuki, R. Murakami, M. Shibata, J. Sugimoto, *Eur. J. Org. Chem.* **2017**, 159–174.

Received: June 28, 2018